
Article:
Perez, JPH, Freeman, HM orcid.org/0000-0001-8242-9561, Brown, AP orcid.org/0000-0001-9692-2154 et al. (5 more authors) (2020) Direct Visualization of Arsenic Binding on Green Rust Sulfate. Environmental Science and Technology, 54 (6). pp. 3297-3305. ISSN 0013-936X

https://doi.org/10.1021/acs.est.9b07092

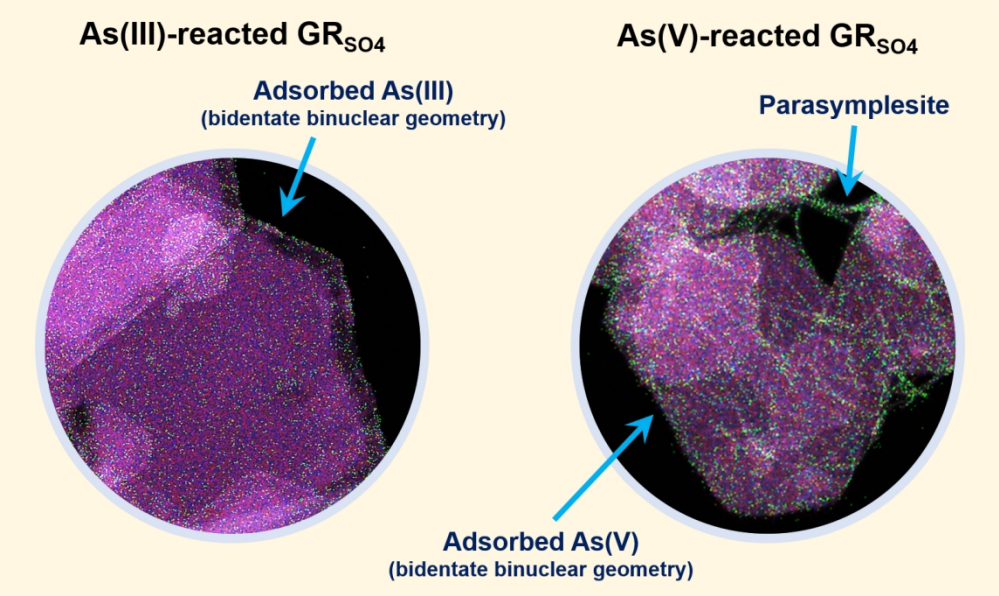

270x161mm (150 x 150 DPI)

Direct visualization of arsenic binding on green rust sulfate

Jeffrey Paulo H. Perez,*[,†,‡] Helen M. Freeman,[†,§] Andy P. Brown,[§] Case M. van Genuchten,[‖,¶] Knud Dideriksen,[‖,⊥] Mark S'ari,[§] Dominique J. Tobler,[⊥] Liane G. Benning[†,‡,Δ]

[†] GFZ German Research Center for Geosciences, Telegrafenberg, 14473 Potsdam, Germany

[‡] Department of Earth Sciences, Freie Universität Berlin, 12249 Berlin, Germany

[§] School of Chemical and Process Engineering, University of Leeds, Leeds LS2 9JT, United Kingdom

[‖] Geological Survey of Denmark and Greenland (GEUS), 1350 Copenhagen, Denmark

[¶] Department of Earth Sciences, Utrecht University, 3584 CB Utrecht, The Netherlands

[⊥] Nano-Science Center, Department of Chemistry, University of Copenhagen, 2100 Copenhagen, Denmark

[Δ] School of Earth and Environment, University of Leeds, Leeds LS2 9JT, United Kingdom

*Corresponding author: jpperez@gfz-potsdam.de

ABSTRACT

'Green rust' (GR), a redox-active Fe(II)-Fe(III) layered double hydroxide, is a potential environmentally relevant mineral substrate for arsenic (As) sequestration in reduced, subsurface environments. GR phases have high As uptake capacities at circum-neutral pH conditions, but the exact interaction mechanism between GR phases and As species are still poorly understood. Here, we documented the bonding and interaction mechanisms between GR sulfate and As species [As(III) and As(V)] at anoxic and circum-neutral pH conditions through scanning transmission electron microscopy (STEM) coupled with energy dispersive X-ray (EDX) spectroscopy, and combined it with synchrotron-based X-ray total scattering, pair distribution function (PDF) analysis and As K-edge X-ray absorption spectroscopy (XAS). Our highly spatially resolved STEM-EDX data revealed that the preferred adsorption sites of both As(III) and As(V) are at GR crystal edges. Combining this data with differential PDF and XAS allowed us to conclude that As adsorption occurs primarily as bidentate binuclear (^{2}C) inner-sphere surface complexes. In the As(III)-reacted GR sulfate, no secondary Fe-As phases were observed. However, authigenic parasymplesite (ferrous arsenate nanophase), exhibiting thread-like morphology, formed in the As(V)-reacted GR sulfate and acts as an additional immobilization pathway for As(V) (~87% of immobilized As). We demonstrate that only by combining high resolution STEM imaging and EDX mapping with bulk (differential) PDF and EXAFS data can one truly determine the de facto As binding nature on GR surfaces. More importantly, these new insights into As-GR interaction mechanisms highlight the impact of GR phases on As sequestration in anoxic subsurface environments.

INTRODUCTION

'Green rust' (GR) phases are redox-active layered double hydroxides (LDHs), consisting of positively-charged Fe(II)-Fe(III) hydroxide layers separated by negatively-charged hydrated interlayers with anions (e.g., Cl^-, SO_4^{2-}, CO_3^{2-}),[1] and occasionally monovalent cations.[2-3] GR phases have been observed as steel corrosion products;[4] but their prevalence in many natural anoxic and suboxic environments, for example in gley soils,[5-6] groundwaters,[7] ferruginous lakes,[8-10] mofette sites[11] and mine drainage sites,[12-13] are increasingly recognized. GR phases are nanoparticulate and have a point of zero charge around pH 8,[14] and are often present in reduced and slightly oxidized subsurface environments where they can act as essential mineral substrates for the removal of toxic oxyanions.[15-17]

Among the most toxic oxyanions, arsenic (As) is often found in high concentrations in drinking and groundwaters where it poses a significant global environmental and public health concern.[18-19] Concentration of As in contaminated natural waters can be as high as 5,000 μg L^{-1}, while mining-influenced environments (e.g., groundwaters affected by mine drainage) can reach concentrations up to 850,000 μg L^{-1}.[20] These concentrations are of concern, especially because the World Health Organization provisional limit for As in drinking water is 10 μg L^{-1},[19] and target concentrations are even lower in some countries (e.g., Denmark, 5 μg L^{-1};[21] Netherlands, 1 μg L^{-1}).[22-23]

GR phases are among the most effective Fe (oxyhydr)oxides for As sequestration under anoxic conditions and circum-neutral to slightly alkaline pH.[24] We have shown that synthetic GR sulfate can adsorb up to 160 mg As(III) and 105 mg of As(V) per g solid, and that geochemical factors such as pH, ionic strength and the presence of co-existing ions can greatly affect As uptake.[25] We have also recently demonstrated that anoxic aging of As-bearing GR carbonate leads to the incorporation of As into the magnetite transformation product, which affects aqueous As concentrations.[26]

While the geochemical controls on As uptake and/or re-release have been identified, a clear mechanistic understanding of the As-GR interaction process is still lacking. Several studies have proposed mechanisms for the interactions between GR phases and As species using synchrotron X-ray absorption spectroscopy (XAS).[27-29] X-ray absorption near-edge structure (XANES) data from these studies revealed that when starting with pure synthetic GR, As redox transformation was not observed. Based on the extended X-ray absorption fine structure (EXAFS) spectra of As-reacted GR, these studies

suggested that both As(III) and As(V) adsorb to GR edges primarily as bidentate binuclear (^2C) inner-sphere surface complexes.[28,30-31] However, in systems where GR was only present as a metastable intermediate phases, partial As(V) reduction to As(III) has been reported.[26,32-33] Two other studies suggested that As(III) may form unique multi-nuclear oligomeric surface complexes on GR surfaces.[29,34] In these experiments, As was either adsorbed or coprecipitated and the EXAFS results suggested a coordination environment with two As(III) pyramids binding to adjacent FeO_6 octahedra in a monodentate mononuclear ^1V geometry forming an As-As dimer by sharing an oxygen atom. This suggested potential polymerization of As(III) at the GR particle edges is favorable since it could lead to a higher removal efficiency of the highly toxic and mobile As(III) from contaminated sediments and groundwater.

These EXAFS data have indeed helped identify possible local bonding environments of sorbed As species on mineral surfaces such as GR phases. However, the lack of independent, cross-confirming analyses to validate these molecular-scale interactions inferred from EXAFS led, not surprisingly, to contrasting interpretations of the nature of immobilized As on GR surfaces (cf. Wang et al.[29], Jönsson & Sherman[28]). Pinpointing any nano-scale interactions between mineral surfaces and sorbed species requires complementary analysis both at high spatial resolution as afforded by (scanning) transmission electron microscopy (S/TEM)[35-39] and highly energy resolved structural information from pair distribution function (PDF) analysis.[40-41] To truly derive mechanistic information about As-GR interactions, we assert that direct observations of mineral-metal surface interactions by S/TEM imaging and elemental mapping, combined with EXAFS-derived bonding environment and structural information from PDF analysis are needed.

In this study, we document just that; we analyzed the interactions between As species [As(III) and As(V)] and synthetic GR sulfate at anoxic and circum-neutral pH conditions, and directly visualized the morphological changes and quantified the differences in elemental As distributions at GR binding sites through energy dispersive X-ray (EDX) mapping and high angle annular dark field (HAADF) imaging in STEM. This direct visualization was complemented by local structure data from high energy X-ray total scattering and PDF analysis and As oxidation state and local bonding environment data from As K-edge X-ray absorption spectroscopy (XAS). Based on these complementary datasets, we

documented the unprecedented differences and similarities in As(III) and As(V) adsorption onto GR surfaces.

MATERIALS AND METHODS

General methods

All glass- and plastic-wares were cleaned in 5 M HCl for 24 h, followed by thorough rinsing with deionized water (Milli-Q, resistivity ~18.2 MΩ·cm). All chemicals were ACS reagent grade from Sigma-Aldrich and Acros Organics and were used as received. Stock solutions were prepared inside an anoxic, vinyl-walled glovebox (97% N_2, 3% H_2, Coy Laboratory Products, Inc.) using deoxygenated, deionized water, which was obtained by purging the water with O_2-free argon at 90 °C for at least 4 h.

GR synthesis and bulk adsorption experiments

GR sulfate was synthesized following a modified co-precipitation method by Géhin et al.[42] by titrating a mixed solution of $(NH_4)_2Fe(SO_4)_2 \cdot 6H_2O$ and $Fe_2(SO_4)_3$ (Fe(II)/Fe(III) ratio = 3) with NaOH until pH ~8.[25,43] The freshly-precipitated GR slurries (~27 mM Fe_{tot}) were added with either As(III) or As(V) solution ($[As]_{initial} \approx 6.7$ mM) at pH ~7 and were reacted for 5 days. The amount of adsorbed As was determined by inductively couple plasma optical emission spectroscopy (ICP-OES Varian 720ES) following a method described in Perez et al.[25]. Further information can be found in the Supporting Information (Text S1).

Material characterization

The As-reacted GR solids were analyzed by a suite of laboratory- and synchrotron-based characterization techniques to determine their structure and composition, particle sizes and morphologies, and As oxidation state and bonding environment. All sample preparations for material characterization were done inside an anoxic glovebox, either with a 97% N_2/3% H_2 (Coy) or an argon (MBRAUN) atmosphere. Detailed information on sample preparation to prevent oxidation and on solid characterization can be found in the Supporting Information (Text S1).

The morphology, structure, size and elemental composition of the As-reacted GR samples were characterized by S/TEM. HAADF-STEM images and EDX spectra and maps were recorded using an FEI Titan^3 Themis G2 S/TEM operating at 300 kV with an FEI Super-X 4-detector EDX system, a Gatan One-View CCD and a Gatan Quantum 965 ER imaging filter. The specimens were stable under the electron beam and no significant changes in morphology or crystal structure were observed during data acquisition (< 15 min per region of interest).[44] Principal component analysis (PCA) and non-negative matrix factorization (NMF) were carried out on the acquired EDX maps to separate different phases present in the spectral image. The analyses were carried out using the Python library HyperSpy[45] by loading the spectral image into HyperSpy and then cropping the energy signal between 0.1 and 12 keV to remove the large EDX peak found at 0 keV and to reduce the size of the dataset.

The local structure of the solids was investigated using PDF analyses, following synchrotron-based X-ray total scattering analyses. The X-ray total scattering data were collected at beamline 11-ID-B at the Advanced Photon Source (Argonne National Laboratory, USA). Differential PDFs (d-PDFs) were obtained by subtracting the PDF of pure GR from the As-reacted samples to isolate atomic correlations arising from adsorbed species and/or surface precipitates. Prior to subtraction, the individual PDFs were normalized to have identical intensities at the first neighbor Fe-O pairs (~2 Å).

XAS analyses were carried out to determine the oxidation state and local bonding environment of immobilized As in the solid samples. Arsenic K-edge XAS data were collected at BM23 of the European Synchrotron Radiation Facility (ESRF, Grenoble, France).[46] For reference materials, we used spectra of freshly synthesized As-adsorbed ferrihydrite,[32] As-adsorbed GR sulfate[31] and parasymplesite.[47] Details of these synthesis methods, as well as any complementary characterization of these reference materials, can be found in the Supporting Information (Text S1). All data reduction and analysis of the XAS spectra were performed using the SIXPack software.[48]

RESULTS AND DISCUSSION

Localization of immobilized arsenic and formation of secondary arsenic phase

Freshly-precipitated GR particles form thin hexagonal plates, about 0.1-1 μm in diameter and 20-50 nm thick (Figure S1).[44] After 5 days of reaction with As species, GR removed almost all (≥98% removal efficiency) of the initially added As species, consistent with our previous work.[25]

HAADF-STEM images of As(III)-reacted GR platelets revealed a bright rim (~10 nm wide, see arrows in Figure 1a) around the crystals, which was separated from the remaining GR particle by a darker band (ca. 20 to 30 nm wide, indicated by dashed lines). HAADF contrast correlates with particle thickness and atomic number (typical $Z^{\sim 1.7}$),[49] and thus STEM-EDX analysis was used to confirm whether or not the dark bands and bright rims were simply a different thickness compared to the rest of the GR platelet or indeed compositionally different. The EDX maps (Figure 1b-d) and integrated intensity line profiles (Figure 1g) across the darker bands confirmed that the absolute Fe, O and S signal intensities decreased significantly within the band compared to the bulk GR crystal. The relative intensities of Fe and O remained constant while there is an apparent decrease in S signal intensity at the dark band and the rim. This decreased S signal is a consequence of the combined effect of low Z value and low mass fraction of S in the GR_{SO4} structure (~4-5 wt. %).[2,42] Overall, these suggest that the GR platelets were thinner in the darker bands, which is best explained by crystal dissolution. The integrated As intensities (Figure 1g) were remarkably higher at the very rim, confirming that As was preferentially adsorbed at GR crystal edges (Figure 1e,f).[25,28-29] We suggest that the GR crystal can partially dissolve and form the dark bands because the amount of adsorbed As(III) does not fully cover all adsorption sites at the crystal edges. It is also noteworthy that the dark dissolution bands are not continuous since some crystal edge areas exhibited substantially more As than other areas (green arrows in Figure 1a; red/yellow hotspots in Figure 1h), meaning the adsorbed As protected the underlying crystal from further dissolution.

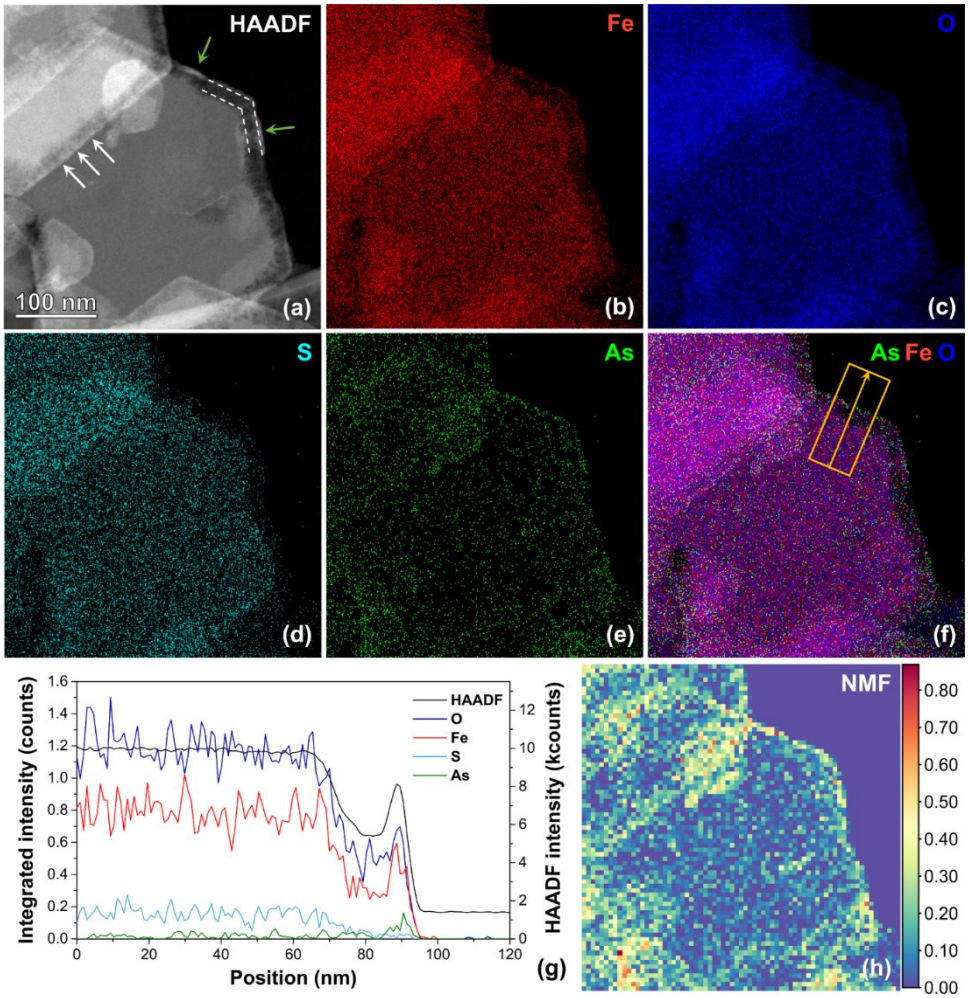

Figure 1. (a) HAADF-STEM image of As(III)-reacted GR_{SO4} and the corresponding EDX elemental maps: (b) Fe (red); (c) O (blue); (d) S (cyan); (e) As (green); and (f) combined As, Fe and O. (g) The HAADF and EDX signal intensity profile showing the changes in concentration of Fe, O, S and As along the integrated line drawn across the marked area in yellow in (f). (h) Non-negative matrix factorization (NMF) loading revealing As-rich areas in the GR particles.

In contrary, the As(V)-reacted GR platelets did not exhibit any dark bands/bright rims, but instead they were characterized by small dissolution cracks (Figure S2) and secondary thread-like structures (Figure 2a and S2) that were closely associated with the GR platelets. EDX maps revealed no change in the bulk As(V)-reacted GR composition as evidenced by the near-homogeneous distribution of Fe, O and S across the GR crystal (Figure 2f,g). The thread-like structures were enriched in As (Figure 2e,f), suggesting that these secondary nanostructures were an As-bearing precipitate. Similar to As(III), the As EDX map of the As(V)-reacted GR also showed higher signals at particle edges (see Figure S2), suggesting that these are the preferred adsorption sites for As(V) on GR.[29-30]

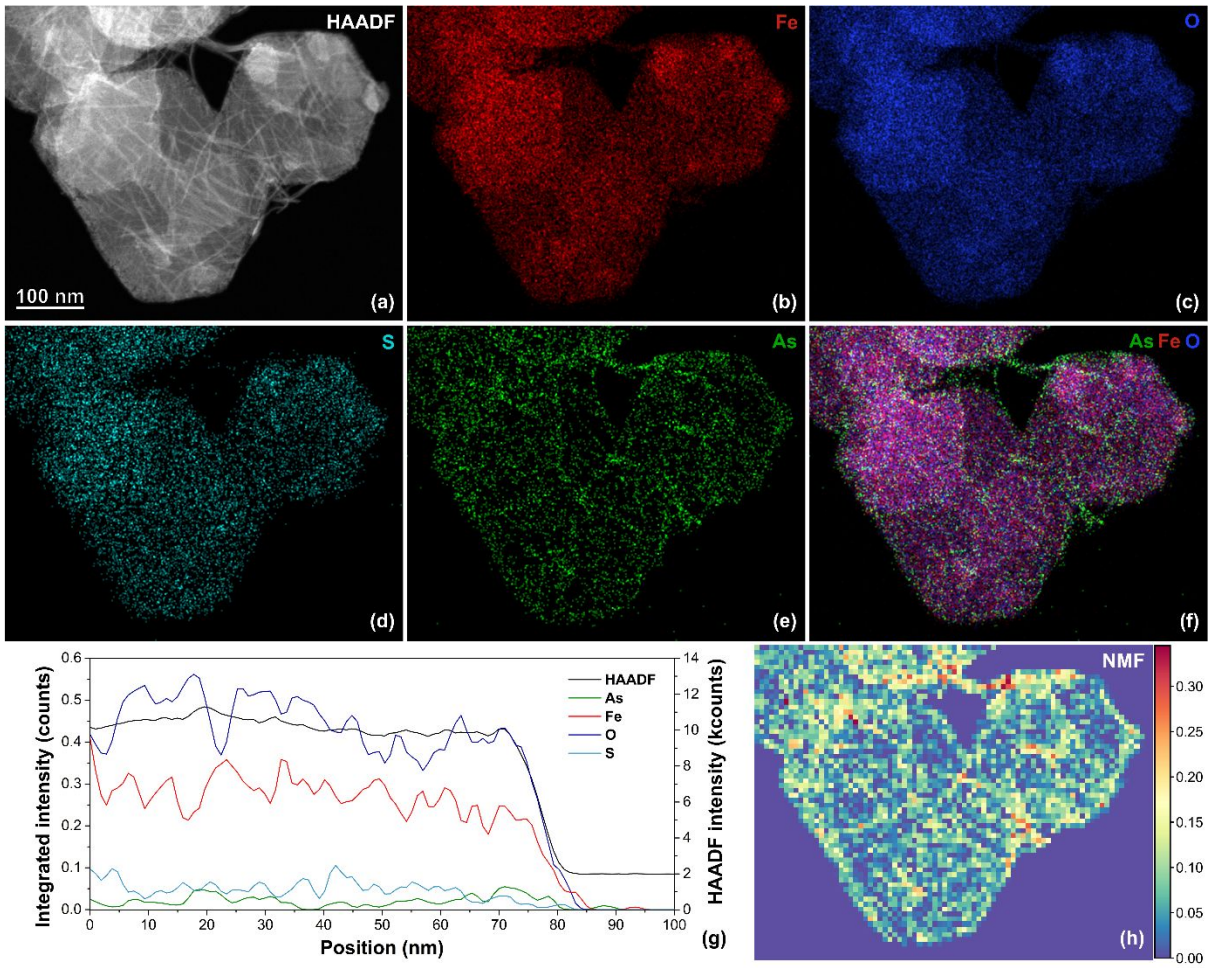

Figure 2. (a) HAADF-STEM image of As(V)-reacted GR_{SO4} and the corresponding EDX elemental maps: (b) Fe (red); (c) O (blue); (d) S (cyan); (e) As (green); and (f) combined As, Fe and O. (g) The HAADF and EDX signal intensity profile showing the changes in concentration of Fe, O, S and As along the integrated line drawn across the marked area in yellow in (f). (h) NMF loading revealing As-rich areas in the GR particles.

Principal component analysis (PCA) and non-negative matrix factorization (NMF) of the EDX data[50] helped to identify differences in the signals within the elemental maps (Figure 1f and 2f; Text S1). In the As(III)-reacted GR data, we identified 4 NMF components (i.e., different phases): (i) bulk GR crystal without As signal (Figure S3a), (ii) substrate carbon film (Figure S3b), (iii) GR crystal edges with high As peak intensity (Figure 1h, S3c) and (iv) bulk GR crystal with relatively small As peak intensity (Figure S3d). The As peak intensity at the GR edges (3rd component) was up to ~7-fold higher compared to that in the GR bulk crystal (4th component), confirming that As(III) is preferentially bound

at the GR edges. For the As(V)-reacted GR, 3 NMF components were extracted: (i) bulk GR crystal without As contributions (Figure S4a), (ii) GR crystal edges and thread-like structures with high relative As peak intensity (Figure 2h, S4b) and (iii) bulk GR crystal with a relatively low As peak intensity (Figure S4c). The high As signal in the thread-like structures clearly indicated that, besides the As adsorbed at the GR edges, a secondary As-bearing precipitate formed.

Structure of As-reacted green rust and formed secondary arsenic phase

To determine what this secondary As-rich phase was, we employed high energy X-ray diffraction (XRD) analyses. The I(Q) patterns of the As(V)-reacted GR samples confirmed the STEM observations and revealed that the secondary As-bearing phase was parasymplesite[51-52] (arrows in Figure 3a, middle pattern). To confirm the structure of this new phase, we prepared synthetic parasymplesite using a co-precipitation method,[47] and characterized it using S/TEM and conventional XRD analyses (see Figure S5). The morphology of the synthetic parasymplesite is also thread/needle-like (Figure S5a,b), and equivalent to the secondary phase associated with the As(V)-reacted GR plates (Figure 2). This implies that the parasymplesite associated with our As(V)-reacted GR must have formed through the partial dissolution (Figure S2a,d) of the initial As(V)-GR, releasing As(V) and Fe^{2+}.[53-54] This released Fe^{2+} then formed a ternary complex with the As(V) surface complexes leading to surface precipitation of parasymplesite.[55-56] A similar process was previously reported in experiments when As species were reacted with ferrihydrite,[53] schwertmannite[55] and siderite.[56]

These observations were cross-confirmed by PDF analyses of the high energy X-ray total scattering data, where the G(r) of the pure and As-reacted GR samples exhibited similar structural coherence domains of 80 Å (Figure 3b), with the decay in peak oscillation mainly reflecting instrumental dampening (Figure S7a). In all GR patterns, the peak at ~1.49 Å corresponds to the S-O bond of the SO_4^{2-} anions in the GR interlayer, while the peak at 1.69 Å in the As(V)-GR was attributed to the As^V-O pair of $HAs^VO_4^{2-}$. Meanwhile, the peaks at r-values between 2 and 4 Å (Figure 3b) correspond to atomic correlations within the Fe hydroxide sheet of GR. For example, the intense peaks at ~2.08 and ~3.18 Å match the first neighbor octahedrally-coordinated Fe-O and edge-sharing Fe-Fe pairs, respectively. The positions of these peaks are similar for the pure and As-reacted GR samples,

confirming that the local coordination environment of Fe within the GR sheets did not change significantly during the reaction.

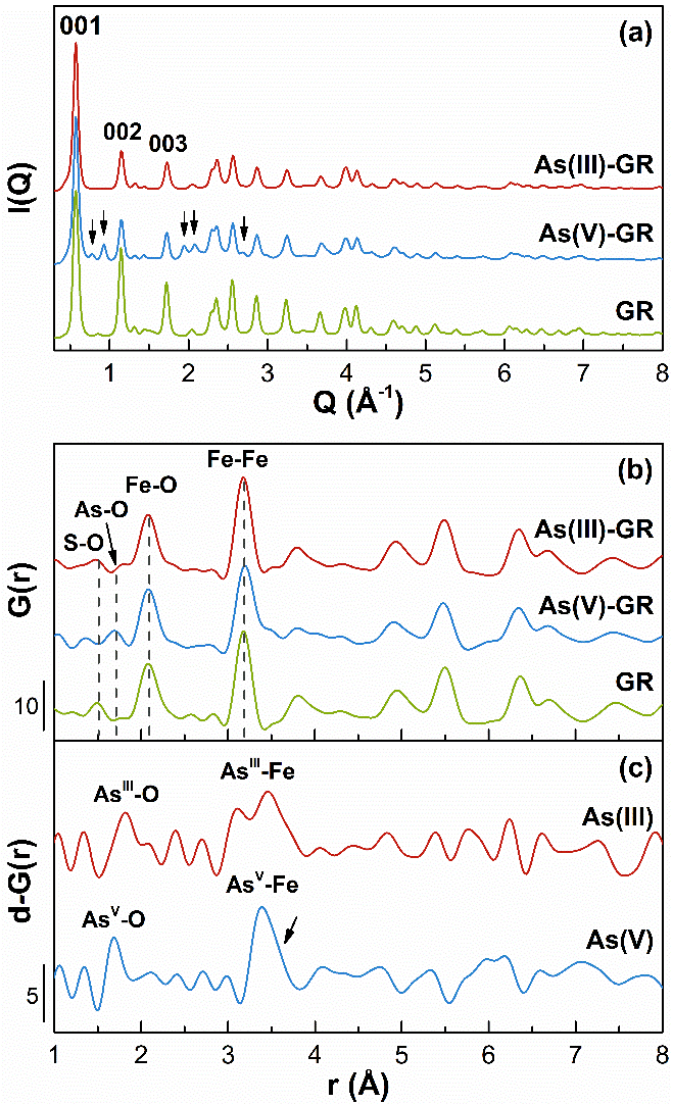

Figure 3. (a) High energy XRD patterns [I(Q)] of pure and As-reacted GR. All peaks represent GR, except those marked with arrows, which correspond to parasymplesite [$Fe^{II}_3(As^{V}O_4)_2{\cdot}8H_2O$]. The relative intenstity of GR (*00l*) peaks change after reaction with As, possibly as a result of shifts in the electron density along the *c*-axis; (b) PDFs [G(r)] of the low r-value region showing the short-range structure of the GR samples. The full PDFs are shown in Figure S7a. (c) The differential PDFs (d-PDFs) [d-G(r)] were obtained by subtracting the PDF of pure GR from the As-reacted samples to isolate atomic correlations arising from adsorbed species and/or surface precipitates.

In the PDFs, slight peak broadening and some asymmetry is visible in the Fe-Fe peak at ~3.18 Å of the As-reacted GRs (Figure 3b). This may be attributed to atomic correlations from adsorbed As, and

from parasymplesite in the case of As(V)-reacted GR. We calculated the differential PDFs, which have proven to be a very useful approach for identifying surface complexes on minerals[40-41] or surface coatings on nanoparticles.[57] The first clear peak in our d-PDF of As(III)-GR (red pattern, Figure 3c) matches the As-O atomic pair (r ≈ 1.80 Å) of the $As^{III}O_3$ pyramid, while the peak at ~3.45 Å fit with As^{III}-Fe atomic correlation for bidentate binuclear ^2C inner-sphere surface complexes.[28] The d-PDF of As(V)-GR (blue pattern, Figure 3c), instead, shows a peak (r ≈ 1.69 Å) that matches the atomic distance of As-O in tetrahedral As^VO_4. In addition, a second asymmetric peak (r ≈ 3.39 Å; arrow in Figure 3c) indicated the presence of multiple As(V)-Fe distances. We know from the complementary analyses that this sample contains parasymplesite, and thus this peak was fitted with three sub-peaks (based on the crystal structure from Runčevski et al.[51], Figure S7b), yielding r-values of ~3.30, ~3.39 and ~3.52 Å. Noteworthy that the peak at ~3.4 Å also matches the As^V-Fe pair distance for ^2C surface complexes (~3.4 Å).[27-29]

Bonding environment of immobilized arsenic species

Although STEM and PDF analyses gave us highly quantitative information about the structure and adsorbed species of the As(III)- and As(V)-reacted GR, we combined these results with As K-edge XAS data (i.e., XANES and EXAFS) to determine if any changes in the As oxidation state occurred during the 5-day reaction with GR (Figure 4a) and confirm the As adsorption geometry using shell-by-shell fits (Figure 4c). Our XANES observations (Figure 4a) support previous studies that have shown that GR cannot oxidize As(III) or reduce As(V).[27-29,31] It is noteworthy, however, that As(III) oxidation to As(V) under anoxic conditions has been reported for other iron-bearing minerals such as siderite,[56] Fe(II)-bearing nontronite,[58-59] lepidocrocite[60] and goethite.[61] Furthermore, As(V) reduction has been observed during Fe^{2+}-catalyzed transformations of Fe-bearing minerals wherein GR has been found as an intermediate phase.[32-33]

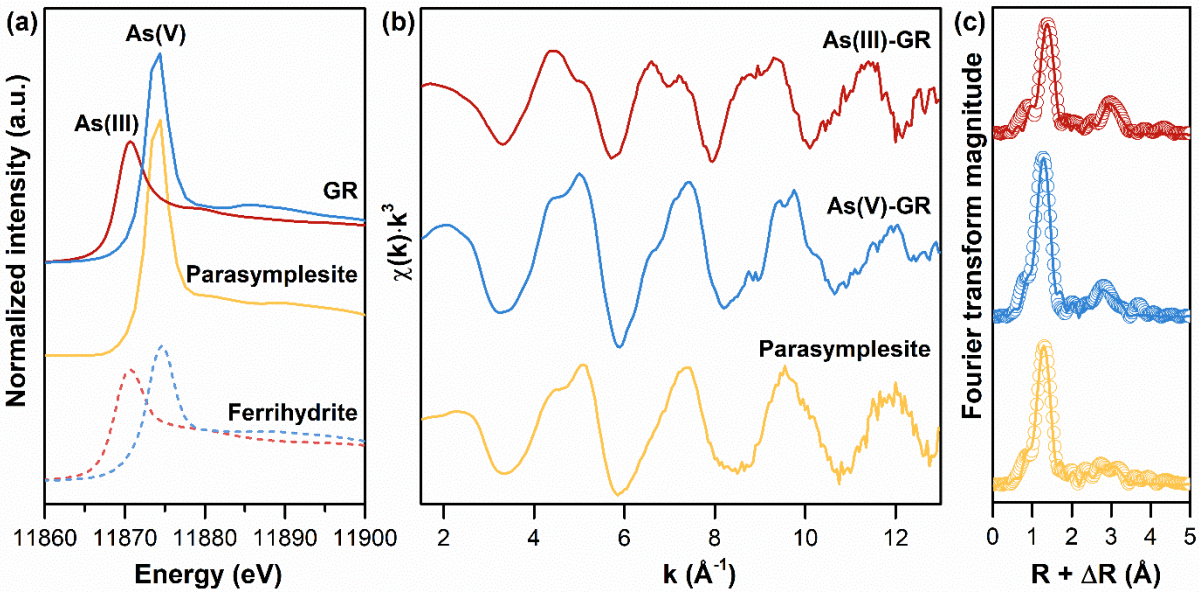

Figure 4. Arsenic K-edge XAS of As-reacted GR samples recorded at ~77 K. (a) XANES spectra of the reacted solids and the reference materials (i.e., parasymplesite, As(III) and As(V) adsorbed onto ferrihydrite); (b) k^3-weighted $\chi(k)$ EXAFS spectra; and (c) Fourier-transformed EXAFS spectra. The shell-by-shell fitting output (solid line) is superimposed on the experimental data (open circles) and the shell-by-shell fitting results are given in Table 1.

The first-neighbor contribution to the EXAFS fit for As(III)-GR spectra is consistent with As-O atomic correlation in an $As^{III}O_3$ pyramid,[62] with a coordination number (CN) of ~3 and an interatomic distance (R) of 1.77 ± 0.01 Å. For the second-neighbor contribution, three possible geometries were considered in the fit corresponding to inner-sphere surface complexes of As(III) at the GR particle edges (see also Figure S7): (1) monodentate mononuclear ^1V geometry ($R_{As\text{-}Fe} \approx 3.5$ Å); (2) bidentate binuclear ^2C geometry ($R_{As\text{-}Fe} \approx 3.4$ Å); and (3) mononuclear edge-sharing ^2E geometry ($R_{As\text{-}Fe} \approx 3.0$ Å).[63] The As-Fe path corresponding to a monodentate ^1V geometry was not supported by the fit, which yielded unrealistically high $R_{As\text{-}Fe}$ values (see Table S1). The predicted dominant second-neighbor contribution was the bidentate ^2C geometry ($R_{As\text{-}Fe} = 3.40 \pm 0.01$ Å, $CN_{As\text{-}Fe} = 3.2 \pm 0.4$), which also complements our d-PDF data for As(III)-GR (Figure 3c). This fit yielded physically reasonable parameters with low fit-derived standard errors (reduced chi-square χ^2) and a low R-factor (≤ 0.05, see Table 1).[64] A second As-Fe path corresponding to the edge-sharing ^2E geometry was also added but did not result in a statistically improved fit (i.e., the decrease in reduced χ^2 with two As-Fe paths did not pass the test of statistical significance),[64] although an atomic pair at 3.1 Å was observed in the d-PDF (Figure 3c).

Multi-nuclear As(III) dimers (i.e., two As(III) pyramids bound to adjacent FeO_6 octahedra in ^1V geometry) have also been previously reported to form on GR surfaces. We attempted to fit an As-As path consistent with an As(III) dimer ($R_{As-As} \approx 3.3$ Å, $CN_{As-As} = 1$). This fit, however, yielded an overlap of the two atomic correlations (i.e., As-Fe and As-As) near ~3.4 Å, indicating that the fit did not support the presence of both As-Fe atomic pairs and As-As dimers. When the second-neighbor contribution was first fitted with the edge sharing ^2E geometry instead of the ^2C geometry and an As(III) dimer was added in a second fitting step, the resulting fit yielded reasonable fitting parameters. However, based on previous work,[29,34] an As-As dimer requires two adjacent As(III) pyramids bound in the ^1V geometry. Since the ^1V geometry was not accepted by our fits, and considering the geometrical constraints imposed on As(III), when bound in the ^2E geometry, we argue against the presence of both As-Fe and As-As bonds in our data. Therefore, we suggest that the dominant surface complex in the As(III)-reacted GR was present in the ^2C geometry (Table 1), with As(III) dimers and edge-sharing ^2E surface complexes constituting a very minor species, if at all present.

Table 1. Summary of shell-by-shell fitting results for As-reacted GR samples.

Sample	Atomic Pairs	CN	R (Å)	σ^2 (Å^2)	ΔE_0 (eV)	R-factor
As(III)	As-O	2.9 (0.2)	1.77 (0.002)	0.002 (0.0005)	9.8 (0.1)	15.1
	As-O-O	6	1.82(R_{As-O}) = 3.23	σ^2 (As-O)		
	As-Fe	3.2 (0.4)	3.40 (0.01)	0.008		
As(V)	As-O	4.2 (0.3)	1.69 (0.01)	0.002	5.7 (2.1)	509.5
	As-O-O	12	1.82(R_{As-O}) = 3.07	σ^2 (As-O)		
	As-Fe	4.1 (1.7)	3.34 (0.03)	0.008		
	As-Fe	2.0 (3.0)	3.51 (0.08)	0.008		

Note: CN - coordination number, R - interatomic distance, σ^2 - mean-squared atomic displacement and ΔE_0 - change in threshold energy. The passive electron reduction factor (S_0^2) was fixed at 1.0. The multiple scattering As-O-O path was constrained geometrically to the single scattering As-O path ($R_{As-O-O} = 1.82\ R_{As-O}$). All fits were carried out from 1 to 4 Å in R+ΔR-space. The number of independent points (N_{IDP}) in the fits was 19.8 and the number of variables (N_{Var}) was 6. Further information can be found in Table S1.

For As(V)-GR, the first-neighbor contribution to the EXAFS fit corresponds to the As-O atomic correlation for tetrahedral $As^VO_4^{3-}$ ($R_{As-O} = 1.69 \pm 0.01$ Å, $CN_{As-O} = 4.2 \pm 0.3$). Again, there are two possible bonding geometries (see Figure S7) for the second-neighbor contribution: (1) ^1V geometry ($R_{As-Fe} \approx 3.5$ Å) and (2) ^2C geometry ($R_{As-Fe} \approx 3.4$ Å). In addition to these, atomic correlations from the As-Fe pairs of parasymplesite ($R_{As-Fe} \approx 3.30$, 3.34, 3.45 Å, each with $CN_{As-Fe} = 2$) have to also be

297 considered.[51] Similar to As(III), the fits revealed that ^2C surface complexes ($R_{As\text{-}Fe}$ = 3.35 ± 0.02 Å,
298 $CN_{As\text{-}Fe}$ = 2.9 ± 1.0) were the dominant bonding geometry for As(V), which confirms our d-PDF
299 observations (Figure 3c). The calculated $CN_{As\text{-}Fe}$ is higher than the expected value for a ^2C geometry.
300 This can be attributed to the additional As-Fe pair of parasymplesite, and therefore, a second As-Fe path
301 was added to account for the precipitated parasymplesite ($R_{As\text{-}Fe}$ ≈ 3.3 Å, $CN_{As\text{-}Fe}$ ≈ 5). This resulted in
302 a good R-factor, yet not statistically significantly better fit compared to the initial sole ^2C geometry
303 fitting parameter values (Table 1): (i) $R_{As\text{-}Fe1}$ = 3.34 ± 0.03 Å, $CN_{As\text{-}Fe1}$ = 4.1 ± 1.7 and (ii) $R_{As\text{-}Fe2}$ = 3.51
304 ± 0.08 Å, $CN_{As\text{-}Fe2}$ = 2.0 ± 2.0. Hence, we employed a linear combination fitting (LCF) approach of the
305 EXAFS data using As(V)-adsorbed GR[31] and parasymplesite references, and this revealed that ~87%
306 of As(V) in the solids were present as parasymplesite, while the remaining ~13% accounts for the
307 adsorbed As(V) species (see LCF results and statistics in Table S2 and Figure S8).
308 Our EXAFS results cross-correlate and confirm the STEM-EDX and d-PDF observations that the
309 thread-like phase (Figure 2) was indeed the secondary As-rich precipitate parasymplesite. This
310 secondary phased formed through a so far not described mechanism. Upon reaction of the GR with the
311 As(V) solution, GR was partially dissolved and released some Fe^{2+}, which then combined with the
312 largest proportion of the initial aqueous As(V) and precipitated as the thread-like secondary
313 parasymplesite.
314
315 **Environmental implications**
316 Our high-resolution STEM images and elemental maps combined with the PDF and XAS data
317 documented new, nano-scale information about the mechanisms of As binding onto GR particle edges
318 (Figure 1 and 2). Both As(III) and As(V) adsorbed to GR particle edges primarily as bidentate binuclear
319 ^2C inner-sphere surface complexes (Figure 3 and 4). Although not unequivocal, our data also does not
320 suggest the formation of multi-nuclear As(III) oligomers on GR_{SO4} edges at circum-neutral pH, which
321 is contrary to findings on GRs intercalated with other anions (e.g., chloride or carbonate).[29,34] However,
322 it is possible that the formation of As(III) oligomers at the GR_{SO4} surfaces can be promoted at other
323 conditions (i.e., pH, ionic strength). For example, we have shown in our previous work that the
324 maximum adsorption capacity of As(III) is ~2.2-fold higher at slightly alkaline pH conditions (pH 8-9)

compared to circum-neutral pH.[25] We also showed that parasymplesite (a ferrous arsenate nanophase), closely associated to the GR platelets, formed through the partial dissolution of GR in the As(V)-reacted sample. Although the GR sulfate used in this study clearly can efficiently sequester As species, changes in pH and redox conditions can cause potential re-release of As back into the environment. However, the re-sequestration of As through the precipitation of secondary As-bearing minerals such as parasymplesite, which themselves have a high As content (up to ~25 wt. %), are highly stable and poorly soluble phases.[65] Thus, indeed, authigenic parasymplesite can minimize As re-release, across a wide range of dynamic geochemical conditions, because it is a more stable immobilized phase. Parasymplesite can therefore further decrease the mobility of As in anoxic, Fe^{2+}-rich groundwater and sediments. Overall, our results provide new crucial mechanistic insights into how redox-active minerals, such as GR phases, interact with As species and their potentially critical role in controlling the toxicity and mobility of As in contaminated subsurface environments.

ASSOCIATED CONTENT

Supporting Information

The Supporting Information is available free of charge on the ACS Publications Web.

Mineral synthesis and characterization methods, STEM images and EDX analyses, PDF data, and EXAFS shell-by-shell fitting and LCF results and statistics.

AUTHOR INFORMATION

Corresponding author

*E-mail: jpperez@gfz-potsdam.de

Notes

The authors declare no competing financial interest.

ACKNOWLEDGEMENTS

This project has received funding from the European Union's Horizon 2020 Marie Skłodowska-Curie Innovative Training Network Grant No. 675219. L.G.B and H.M.F. acknowledge the financial support

from the Helmholtz Recruiting Initiative (award number I-044-16-01). TEM access was possible through the Royal Society of Chemistry (RSC) Researcher Mobility Grant (project no. RM1602-226) and Geo.X Travel Grant (Grant No. SO_087_GeoX) awarded to J.P.H.P., and the EPSRC grant EP/M028143/1 at the University of Leeds. C.M.v.G. acknowledges partial funding from an NWO Veni grant (project no. 14400). Use of APS was supported by the U.S. Department of Energy, Office of Science, Office of Basic Energy Sciences, under Contract No. DE-AC02-06CH11357. D.J.T and K.D. acknowledge financial support from the Danish Council for Independent Research (via DANSCATT) for travel to APS, and the assistance of Olaf Borkiewicz and Kevin A. Beyer during X-ray scattering measurements at APS beamline 11-ID-B, Argonne, USA. The As K-edge EXAFS data were collected at the BM23 beamline at ESRF (experiment no. EV-338), and the authors thank Sakura Pascarelli for assistance during beamtime.

References

1. Usman, M.; Byrne, J. M.; Chaudhary, A.; Orsetti, S.; Hanna, K.; Ruby, C.; Kappler, A.; Haderlein, S. B., Magnetite and green rust: Synthesis, properties, and environmental applications of mixed-valent iron minerals. *Chem. Rev.* **2018,** *118* (7), 3251-3304.
2. Christiansen, B. C.; Balic-Zunic, T.; Petit, P. O.; Frandsen, C.; Mørup, S.; Geckeis, H.; Katerinopoulou, A.; Stipp, S. L. S., Composition and structure of an iron-bearing, layered double hydroxide (LDH) – Green rust sodium sulphate. *Geochim. Cosmochim. Acta* **2009,** *73* (12), 3579-3592.
3. Christiansen, B. C.; Dideriksen, K.; Katz, A.; Nedel, S.; Bovet, N.; Sørensen, H. O.; Frandsen, C.; Gundlach, C.; Andersson, M. P.; Stipp, S. L. S., Incorporation of monovalent cations in sulfate green rust. *Inorg. Chem.* **2014,** *53* (17), 8887-8894.
4. O'Loughlin, E. J.; Kelly, S. D.; Kemner, K. M.; Csencsits, R.; Cook, R. E., Reduction of Ag^{I}, Au^{III}, Cu^{II}, and Hg^{II} by Fe^{II}/Fe^{III} hydroxysulfate green rust. *Chemosphere* **2003,** *53* (5), 437-446.
5. Trolard, F.; Génin, J.-M. R.; Abdelmoula, M.; Bourrié, G.; Humbert, B.; Herbillon, A., Identification of a green rust mineral in a reductomorphic soil by Mössbauer and Raman spectroscopies. *Geochim. Cosmochim. Acta* **1997,** *61* (5), 1107-1111.
6. Abdelmoula, M.; Trolard, F.; Bourrié, G.; Génin, J.-M. R., Evidence for the Fe(II)-Fe(III) green rust "fougerite" mineral occurrence in a hydromorphic soil and its transformation with depth. *Hyperfine Interact.* **1998,** *112* (1), 235-238.
7. Christiansen, B. C.; Balic-Zunic, T.; Dideriksen, K.; Stipp, S. L. S., Identification of green rust in groundwater. *Environ. Sci. Technol.* **2009,** *43* (10), 3436-3441.

8. Zegeye, A.; Bonneville, S.; Benning, L. G.; Sturm, A.; Fowle, D. A.; Jones, C.; Canfield, D. E.; Ruby, C.; MacLean, L. C.; Nomosatryo, S.; Crowe, S. A.; Poulton, S. W., Green rust formation controls nutrient availability in a ferruginous water column. *Geology* **2012,** *40* (7), 599-602.
9. Koeksoy, E.; Sundman, A.; Byrne, J. M.; Kappler, A.; Planer-Friedrich, B.; Lohmayer, R.; Halevy, I.; Konhauser, K. O., Formation of green rust and elemental sulfur in an analogue for oxygenated ferro-euxinic transition zones of Precambrian oceans. *Geology* **2019,** *47* (3), 211-214.
10. Vuillemin, A.; Wirth, R.; Kemnitz, H.; Schleicher, A. M.; Friese, A.; Bauer, K. W.; Simister, R.; Nomosatryo, S.; Ordoñez, L.; Ariztegui, D.; Henny, C.; Crowe, S. A.; Benning, L. G.; Kallmeyer, J.; Russell, J. M.; Bijaksana, S.; Vogel, H., Formation of diagenetic siderite in modern ferruginous sediments. *Geology* **2019,** *47* (6), 540-544.
11. Rennert, T.; Eusterhues, K.; De Andrade, V.; Totsche, K. U., Iron species in soils on a mofette site studied by Fe *K*-edge X-ray absorption near-edge spectroscopy. *Chem. Geol.* **2012,** *332–333*, 116-123.
12. Bearcock, J.; Perkins, W.; Dinelli, E.; Wade, S., Fe(II)/Fe(III) 'green rust'developed within ochreous coal mine drainage sediment in South Wales, UK. *Mineral. Mag.* **2006,** *70* (6), 731-741.
13. Johnson, C. A.; Freyer, G.; Fabisch, M.; Caraballo, M. A.; Küsel, K.; Hochella, M. F., Observations and assessment of iron oxide and green rust nanoparticles in metal-polluted mine drainage within a steep redox gradient. *Environ. Chem.* **2014,** *11* (4), 377-391.
14. Guilbaud, R.; White, M. L.; Poulton, S. W., Surface charge and growth of sulphate and carbonate green rust in aqueous media. *Geochim. Cosmochim. Acta* **2013,** *108*, 141-153.
15. Thomas, A. N.; Eiche, E.; Göttlicher, J.; Steininger, R.; Benning, L. G.; Freeman, H. M.; Dideriksen, K.; Neumann, T., Products of hexavalent chromium reduction by green rust sodium sulfate and associated reaction mechanisms. *Soil Syst.* **2018,** *2* (4), 58.
16. O'Loughlin, E. J.; Kelly, S. D.; Cook, R. E.; Csencsits, R.; Kemner, K. M., Reduction of uranium(VI) by mixed iron(II)/iron(III) hydroxide (green rust): Formation of UO_2 nanoparticles. *Environ. Sci. Technol.* **2003,** *37* (4), 721-727.
17. Refait, P.; Simon, L.; Génin, J.-M. R., Reduction of SeO_4^{2-} anions and anoxic formation of iron(II)−iron(III) hydroxy-selenate green rust. *Environ. Sci. Technol.* **2000,** *34* (5), 819-825.
18. Vaughan, D. J., Arsenic. *Elements* **2006,** *2* (2), 71-75.
19. World Health Organization, Guidelines for drinking-water quality: Fourth edition incorporating the first addendum. **2017**.
20. Smedley, P. L.; Kinniburgh, D. G., A review of the source, behaviour and distribution of arsenic in natural waters. *Appl. Geochem.* **2002,** *17* (5), 517-568.
21. Ersbøll, A. K.; Monrad, M.; Sørensen, M.; Baastrup, R.; Hansen, B.; Bach, F. W.; Tjønneland, A.; Overvad, K.; Raaschou-Nielsen, O., Low-level exposure to arsenic in drinking water and incidence rate of stroke: A cohort study in Denmark. *Environ. Int.* **2018,** *120*, 72-80.

22. Ahmad, A.; Bhattacharya, P., Arsenic in drinking water: Is 10 μg/L a safe limit? *Curr. Pollut. Rep.* **2019,** *5* (1), 1-3.
23. Ahmad, A.; Cornelissen, E.; van de Wetering, S.; van Dijk, T.; van Genuchten, C.; Bundschuh, J.; van der Wal, A.; Bhattacharya, P., Arsenite removal in groundwater treatment plants by sequential Permanganate—Ferric treatment. *J. Water. Process. Eng.* **2018,** *26*, 221-229.
24. Su, C.; Wilkin, R. T., Arsenate and arsenite sorption on and arsenite oxidation by iron(II, III) hydroxycarbonate green rust. In *Advances in Arsenic Research*, American Chemical Society: 2005; Vol. 915, pp 25-40.
25. Perez, J. P. H.; Freeman, H. M.; Schuessler, J. A.; Benning, L. G., The interfacial reactivity of arsenic species with green rust sulfate (GR_{SO4}). *Sci. Total Environ.* **2019,** *648*, 1161-1170.
26. van Genuchten, C. M.; Behrends, T.; Dideriksen, K., Emerging investigator series: Interdependency of green rust transformation and the partitioning and binding mode of arsenic. *Environ. Sci.: Process. Impacts* **2019**.
27. Randall, S. R.; Sherman, D. M.; Ragnarsdottir, K. V., Sorption of As(V) on green rust ($Fe_4(II)Fe_2(III)(OH)_{12}SO_4 \cdot 3H_2O$) and lepidocrocite ($\gamma$-FeOOH): Surface complexes from EXAFS spectroscopy. *Geochim. Cosmochim. Acta* **2001,** *65* (7), 1015-1023.
28. Jönsson, J.; Sherman, D. M., Sorption of As(III) and As(V) to siderite, green rust (fougerite) and magnetite: Implications for arsenic release in anoxic groundwaters. *Chem. Geol.* **2008,** *255* (1–2), 173-181.
29. Wang, Y.; Morin, G.; Ona-Nguema, G.; Juillot, F.; Guyot, F.; Calas, G.; Brown, G. E., Evidence for different surface speciation of arsenite and arsenate on green rust: An EXAFS and XANES study. *Environ. Sci. Technol.* **2010,** *44* (1), 109-115.
30. Sherman, D. M.; Randall, S. R., Surface complexation of arsenic(V) to iron(III) (hydr)oxides: structural mechanism from ab initio molecular geometries and EXAFS spectroscopy. *Geochim. Cosmochim. Acta* **2003,** *67* (22), 4223-4230.
31. van Genuchten, C. M.; Behrends, T.; Stipp, S. L. S.; Dideriksen, K., Achieving arsenic concentrations of <1 μg/L by Fe(0) electrolysis: The exceptional performance of magnetite. *Water Res.* **2019**, 115170.
32. Perez, J. P. H.; Tobler, D. J.; Thomas, A. N.; Freeman, H. M.; Dideriksen, K.; Radnik, J.; Benning, L. G., Adsorption and reduction of arsenate during the Fe^{2+}-induced transformation of ferrihydrite. *ACS Earth Space Chem.* **2019,** *3* (6), 884-894.
33. Karimian, N.; Johnston, S. G.; Burton, E. D., Antimony and arsenic behavior during Fe(II)-induced transformation of jarosite. *Environ. Sci. Technol.* **2017,** *51* (8), 4259-4268.
34. Ona-Nguema, G.; Morin, G.; Wang, Y.; Menguy, N.; Juillot, F.; Olivi, L.; Aquilanti, G.; Abdelmoula, M.; Ruby, C.; Bargar, J. R.; Guyot, F.; Calas, G.; Brown, G. E., Arsenite sequestration at the surface of nano-$Fe(OH)_2$, ferrous-carbonate hydroxide, and green-rust after bioreduction of

arsenic-sorbed lepidocrocite by *Shewanella putrefaciens*. *Geochim. Cosmochim. Acta* **2009,** *73* (5), 1359-1381.

35. Ling, L.; Tang, C.; Zhang, W.-x., Visualization of silver nanoparticle formation on nanoscale zero-valent iron. *Environ. Sci. Technol. Lett.* **2018,** *5* (8), 520-525.
36. Huang, X.-y.; Ling, L.; Zhang, W.-x., Nanoencapsulation of hexavalent chromium with nanoscale zero-valent iron: High resolution chemical mapping of the passivation layer. *J. Environ. Sci.* **2018,** *67*, 4-13.
37. Ling, L.; Huang, X.; Li, M.; Zhang, W.-x., Mapping the reactions in a single zero-valent iron nanoparticle. *Environ. Sci. Technol.* **2017,** *51* (24), 14293-14300.
38. Ling, L.; Zhang, W.-x., Visualizing arsenate reactions and encapsulation in a single zero-valent iron nanoparticle. *Environ. Sci. Technol.* **2017,** *51* (4), 2288-2294.
39. Wang, Y.; Morin, G.; Ona-Nguema, G.; Juillot, F.; Calas, G.; Brown, G. E., Distinctive arsenic(V) trapping modes by magnetite nanoparticles induced by different sorption processes. *Environ. Sci. Technol.* **2011,** *45* (17), 7258-7266.
40. Harrington, R.; Hausner, D. B.; Bhandari, N.; Strongin, D. R.; Chapman, K. W.; Chupas, P. J.; Middlemiss, D. S.; Grey, C. P.; Parise, J. B., Investigation of surface structures by powder diffraction: A differential pair distribution function study on arsenate sorption on ferrihydrite. *Inorg. Chem.* **2010,** *49* (1), 325-330.
41. van Genuchten, C. M.; Peña, J., Antimonate and arsenate speciation on reactive soil minerals studied by differential pair distribution function analysis. *Chem. Geol.* **2016,** *429*, 1-9.
42. Géhin, A.; Ruby, C.; Abdelmoula, M.; Benali, O.; Ghanbaja, J.; Refait, P.; Génin, J.-M. R., Synthesis of Fe(II-III) hydroxysulphate green rust by coprecipitation. *Solid State Sci.* **2002,** *4* (1), 61-66.
43. Perez, J. P. H.; Mangayayam, M. C.; Rubio, S. N.; Freeman, H. M.; Tobler, D. J.; Benning, L. G., Intercalation of aromatic sulfonates in 'green rust' via ion exchange. *Energy Procedia* **2018,** *146*, 179-187.
44. Freeman, H. M.; Perez, J. P. H.; Hondow, N.; Benning, L. G.; Brown, A. P., Beam-induced oxidation of mixed-valent Fe (oxyhydr)oxides (green rust) monitored by STEM-EELS. *Micron* **2019,** *122*, 46-52.
45. dela Peña, F.; Prestat, E.; Fauske, V. T.; Burdet, P.; Jokubauskas, P.; Nord, M.; Ostasevivius, T.; MacArthur, K. E.; Sarahan, M.; Johnstone, D. N.; Taillon, J.; Eljarrat, A.; Lähnemann, J.; Migunov, V.; Caron, J.; Mazzucco, S.; Aarholt, T.; Walls, M.; Slater, T.; Winkler, F.; pquinn-dls; Martineau, B.; Donval, G.; McLeod, R.; Hoglund, E. R.; Alxneit, I.; Lundeby, D.; Henninen, T.; Zagonel, L. F.; A., G. *Hyperspy/hyperspy: v1.4.2*, 2019.
46. Mathon, O.; Beteva, A.; Borrel, J.; Bugnazet, D.; Gatla, S.; Hino, R.; Kantor, I.; Mairs, T.; Munoz, M.; Pasternak, S.; Perrin, F.; Pascarelli, S., The time-resolved and extreme conditions XAS

(TEXAS) facility at the European Synchrotron Radiation Facility: the general-purpose EXAFS bending-magnet beamline BM23. *J. Synchr. Radiat.* **2015,** *22* (6), 1548-1554.

47. Johnston, R. B.; Singer, P. C., Solubility of symplesite (ferrous arsenate): Implications for reduced groundwaters and other geochemical environments. *Soil Sci. Soc. Am. J.* **2007,** *71* (1), 101-107.
48. Webb, S. M., SIXpack: a graphical user interface for XAS analysis using IFEFFIT. *Phys. Scr.* **2005,** *2005* (T115), 1011.
49. Bach, D.; Christiansen, B. C.; Schild, D.; Geckeis, H., TEM study of green rust sodium sulphate ($GR_{Na, SO4}$) interacted with neptunyl ions (NpO_2^+). *Radiochimica Acta* **2014,** *102* (4), 279-289.
50. Cacovich, S.; Divitini, G.; Ireland, C.; Matteocci, F.; Di Carlo, A.; Ducati, C., Elemental Mapping of Perovskite Solar Cells by Using Multivariate Analysis: An Insight into Degradation Processes. *ChemSusChem* **2016,** *9* (18), 2673-2678.
51. Runčevski, T.; Makreski, P.; Dinnebier, R. E.; Jovanovski, G., The crystal structure of symplesite. *Z. Anorg. Allg. Chem.* **2015,** *641* (7), 1207-1210.
52. Ito, T.-i.; Minato, H.; Sakurai, K. i., Parasymplesite, a new mineral polymorphous with symplesite. *P. Jpn. Acad.* **1954,** *30* (4), 318-324.
53. Jia, Y.; Xu, L.; Fang, Z.; Demopoulos, G. P., Observation of surface precipitation of arsenate on ferrihydrite. *Environ. Sci. Technol.* **2006,** *40* (10), 3248-3253.
54. Wang, L.; Putnis, C. V.; Hövelmann, J.; Putnis, A., Interfacial precipitation of phosphate on hematite and goethite. *Minerals* **2018,** *8* (5), 207.
55. Carlson, L.; Bigham, J. M.; Schwertmann, U.; Kyek, A.; Wagner, F., Scavenging of As from acid mine drainage by schwertmannite and ferrihydrite: A comparison with synthetic analogues. *Environ. Sci. Technol.* **2002,** *36* (8), 1712-1719.
56. Tian, Z.; Feng, Y.; Guan, Y.; Shao, B.; Zhang, Y.; Wu, D., Opposite effects of dissolved oxygen on the removal of As(III) and As(V) by carbonate structural Fe(II). *Sci. Rep.* **2017,** *7* (1), 17015.
57. Mangayayam, M.; Dideriksen, K.; Ceccato, M.; Tobler, D. J., The structure of sulfidized zero-valent iron by one-pot synthesis: Impact on contaminant selectivity and long-term performance. *Environ. Sci. Technol.* **2019,** *53* (8), 4389-4396.
58. Ilgen, A. G.; Foster, A. L.; Trainor, T. P., Role of structural Fe in nontronite NAu-1 and dissolved Fe(II) in redox transformations of arsenic and antimony. *Geochim. Cosmochim. Acta* **2012,** *94*, 128-145.
59. Ilgen, A. G.; Kruichak, J. N.; Artyushkova, K.; Newville, M. G.; Sun, C., Redox transformations of As and Se at the surfaces of natural and synthetic ferric nontronites: Role of structural and adsorbed Fe(II). *Environ. Sci. Technol.* **2017,** *51* (19), 11105-11114.
60. Wang, L.; Giammar, D. E., Effects of pH, dissolved oxygen, and aqueous ferrous iron on the adsorption of arsenic to lepidocrocite. *J. Colloid Interface Sci.* **2015,** *448*, 331-338.
61. Amstaetter, K.; Borch, T.; Larese-Casanova, P.; Kappler, A., Redox transformation of arsenic by Fe(II)-activated goethite (α-FeOOH). *Environ. Sci. Technol.* **2010,** *44* (1), 102-108.

531 62. Shannon, R. D., Revised effective ionic radii and systematic studies of interatomic distances in
532 halides and chalcogenides. *Acta Crystallogr. A* **1976,** *32* (5), 751-767.
533 63. Ona-Nguema, G.; Morin, G.; Juillot, F.; Calas, G.; Brown, G. E., EXAFS analysis of arsenite
534 adsorption onto two-line ferrihydrite, hematite, goethite, and lepidocrocite. *Environ. Sci. Technol.*
535 **2005,** *39* (23), 9147-9155.
536 64. Kelly, S. D.; Hesterberg, D.; Ravel, B., Analysis of soils and minerals using X-ray absorption
537 spectroscopy. In *Methods of Soil Analysis Part 5—Mineralogical methods*, Ulery, A. L.; Drees, L.
538 R., Eds. Soil Science Society of America: Madison, WI, 2008.
539 65. Raghav, M.; Shan, J.; Sáez, A. E.; Ela, W. P., Scoping candidate minerals for stabilization of
540 arsenic-bearing solid residuals. *J. Hazard. Mater.* **2013,** *263*, 525-532.